Solar thermochemical splitting of water to generate hydrogen

C. N. R. Rao[a,1] and Sunita Dey[a]

Edited by Michael L. Klein, Temple University, Philadelphia, PA, and approved March 16, 2017 (received for review January 4, 2017)

Solar photochemical means of splitting water (artificial photosynthesis) to generate hydrogen is emerging as a viable process. The solar thermochemical route also promises to be an attractive means of achieving this objective. In this paper we present different types of thermochemical cycles that one can use for the purpose. These include the low-temperature multistep process as well as the high-temperature two-step process. It is noteworthy that the multistep process based on the Mn(II)/Mn(III) oxide system can be carried out at 700 °C or 750 °C. The two-step process has been achieved at 1,300 °C/900 °C by using yttrium-based rare earth manganites. It seems possible to render this high-temperature process as an isothermal process. Thermodynamics and kinetics of H_2O splitting are largely controlled by the inherent redox properties of the materials. Interestingly, under the conditions of H_2O splitting in the high-temperature process CO_2 can also be decomposed to CO, providing a feasible method for generating the industrially important syngas ($CO+H_2$). Although carbonate formation can be addressed as a hurdle during CO_2 splitting, the problem can be avoided by a suitable choice of experimental conditions. The choice of the solar reactor holds the key for the commercialization of thermochemical fuel production.

thermochemical H_2O splitting | metal oxides | perovskites | thermochemical CO_2 splitting

The impact of global climate change as well as the likely shortage of fossil fuels demand harvesting of energy using renewable sources. Although solar energy captured by the Earth in an hour is expected to satisfy the energy demand of the world for a year, the high energy density and nonpolluting end product renders hydrogen a viable alternative to fossil fuels (1). In this context, conversion of solar power to H_2 and synfuels with the utilization of renewable H_2O and CO_2 seems to be a sound option. Artificial photosynthesis and photovoltaic-powered electrolysis of water are promising approaches, although their implementation is somewhat restricted because of the low solar-to-fuel conversion efficiency ($\eta_{solar\text{-}to\text{-}fuel}$) of <5% and <15%, respectively (2, 3). The other strategy would be a solar-thermochemical process that provides a high theoretical efficiency and enables large-scale production of H_2 by using the entire solar spectrum (4). Research in thermochemical splitting of H_2O made a beginning in the early 1980s (5, 6) and several thermochemical cycles have been examined. Thermochemical methods come under two main categories, the low-temperature multistep processes and the high-temperature two-step processes. The two-step process involving the thermal decomposition of metal oxides followed by reoxidation by reacting with H_2O to yield H_2 is an attractive and viable process that can be rendered to become an isothermal process. Thermochemical splitting of H_2O at low temperatures (<1,000 °C) is accomplished by a minimum of three steps as dictated by thermodynamic energy constraints (7, 8). In this paper we present the highlights of recent investigations of H_2O splitting by the low-temperature multistep process as well as the high temperature two-step process.

Low-Temperature Multistep Cycles

Low-temperature cycles are advantageous due to low radiative losses and availability of more heat resources, including nuclear waste heat sources. There has been a good deal of research in the past decades in this area and the performance of a few cycles such as the S–I and S–Br cycles as well as Fe–Cl, Hg–Br, and Cu–Cl cycles is noteworthy (5, 9). Although they produce H_2 steadily, these cycles suffer from environmental issues associated with the separation of acid mixtures, decomposition of acids, heavy-metal processing,

[a]Chemistry and Physics of Materials Unit, Council of Scientific and Industrial Research Centre of Excellence, Sheikh Saqr Laboratory, International Centre for Materials Science, Jawaharlal Nehru Centre for Advanced Scientific Research, Bangalore 560064, India

Author contributions: C.N.R.R. designed research; S.D. performed research; C.N.R.R. and S.D. analyzed data; and C.N.R.R. and S.D. wrote the paper.

The authors declare no conflict of interest.

This article is a PNAS Direct Submission.

[1]To whom correspondence should be addressed. Email: cnrrao@jncasr.ac.in.

This article contains supporting information online at www.pnas.org/lookup/suppl/doi:10.1073/pnas.1700104114/-/DCSupplemental.

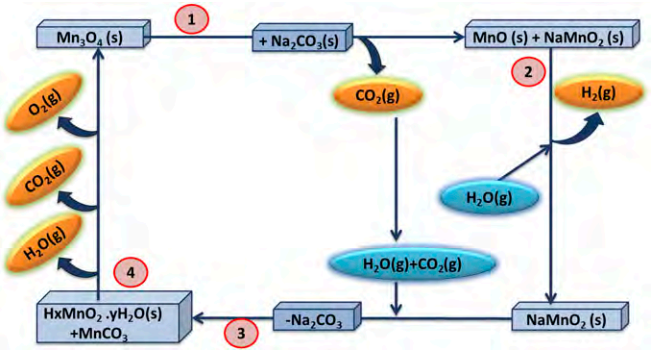

Fig. 1. Schematic presentation of Mn(II)/Mn(III) based low-temperature multistep thermochemical cycle. Reproduced with permission from ref. 13, copyright 2016, Royal Society of Chemistry.

production of toxic or corrosive intermediates, and so on. Even the most-studied sulfur–iodine cycle suffers from the disadvantage of corrosive intermediates (9).

Manganese Oxide-Based Cycles. Transition metal oxide-based multistep cycles have attracted attention. One of these is the four-step cycle based on manganese oxides wherein Mn_2O_3 reduces to MnO with the evolution of O_2 above 1,500 °C, and NaOH then oxidizes Mn(II) back to Mn(III) as $NaMnO_2$(s), with the evolution of H_2 above 600 °C. The best efficiency for this cycle was 74% and 16–22% considering 100% and 0% heat recovery, respectively, as calculated by Sturzenegger and Nuesch (10). Volatility of NaOH above 800 °C and the high Mn_2O_3-to-MnO conversion temperature hinders the practical implementation of this cycle. Instead of NaOH, the use of Na_2CO_3 for the production of H_2 from redox active $MnFe_2O_4$ has been suggested by Tamaura et al. (11), as shown in Eqs. **S1** and **S2**.

Although this cycle closes below 1,000 °C, stoichiometric quantity of O_2 is not evolved due to the incomplete extraction of Na^+ even in the presence of CO_2(g). Modification involving the introduction of Fe_2O_3 as a sacrificial agent has been proposed, but the use of Fe_2O_3 does not close the cycle either (12).

Mn_3O_4-Na_2CO_3-MnO–Based Cycle. In this context, the thermochemical cycle based on Mn_3O_4/MnO oxides proposed by Davis and coworkers is noteworthy (8). The four reactions in this cycle are shown in Fig. 1 (Eqs. **S3**–**S6**). Generation of H_2 occurs at 850 °C in this cycle (Fig. 1) and the cycle is devoid of corrosive products (8). Thermal oxidation of Mn_3O_4 to Mn_2O_3 is thermodynamically unfavorable, but the use of Na_2CO_3 drastically decreases the ΔG and forms MnO(s) and α-$NaMnO_2$(s) at 850 °C with the evolution of CO_2(g), as shown in step 1 (Eq. **S3**) (8, 9). The CO_2 evolution temperature can be decreased drastically (~600 °C) with the use of nanoparticles of Mn_3O_4 and Na_2CO_3 obtained with ball milling (Fig. S1) (13). When nanoparticles of both Mn_3O_4 and Na_2CO_3 are used (Fig. S1), the weight loss occurs sharply below 600 °C, releasing ~100% of CO_2. During step 2 (Eq. **S4**), introduction of H_2O(g) at 850 °C oxidizes MnO to α-$NaMnO_2$ with the evolution of H_2(g) (8). The main hurdle in this cycle is the slow H_2 evolution. The rate of H_2 evolution is significantly enhanced by the use of nanoparticles due to their high surface area (Fig. 2*A*). Thus, ball-milled samples show a high rate of H_2 production soon after the entry of H_2O, with an overall increase of 1.5–2 times in comparison with the bulk samples (13). Interestingly, the use of nanoparticles effectively brings down the H_2 evolution temperature to 750 °C or 700 °C as shown for the 60-min ball-milled (MnNa60) sample in Fig. 2*B*, although the H_2 evolution rate is somewhat slower in comparison with that at 850 °C (Fig. 2). The yield of H_2 at 750 °C is ~40% (over 80 min) with an extended tail due to further H_2 evolution over a period (13).

As shown in Fig. 1, extraction of Na^+ from layered $NaMnO_2$(s) is performed by hydrolysis under a CO_2(g) atmosphere at 80 °C for 3 h (step 3, Eq. **S5**), giving rise to protonic birnessite as the product (8). It has been noted recently that hydrolysis at 50 °C for 1 h extracts Na^+ completely (13). Birnessite reduces to Mn_3O_4 with stoichiometric O_2 evolution (step 4, Eq. **S6**). Investigations of this cycle with other metal oxide (Fe_3O_4 and Co_3O_4)–carbonate pairs (Li_2CO_3 and K_2CO_3) have been conducted by Xu et al. (14) and the H_2 evolution rate was found to vary in the order Fe_3O_4 > Mn_3O_4 > Co_3O_4 and Li_2CO_3 > Na_2CO_3 > K_2CO_3. In this method, the complete extraction of Li^+ ions seems to be impossible and the Fe(III)–Fe(II) reduction temperature is high (~1,150 °C). The manganese oxide-based system, Mn_3O_4/ Na_2CO_3/MnO, seems to be the best combination (14).

Two-Step Thermochemical Processes

The two-step metal oxide process carried out with the aid of solar concentrators eliminates the necessity of separating of H_2 and O_2. The metal oxide (MO_{oxd}) reduces to the metal or to a lower valent metal oxide (MO_{red}) (Eq. **S7**) with the release of O_2(g) during the endothermic step (T_{red}), and in the next step it gets reoxidized (T_{oxd}) on reaction with H_2O (Eq. **S8**), releasing a stoichiometric amount of H_2(g), as shown in Fig. 3.

$T_{red} > T_{oxd}$ is the thermodynamic driving force in the two-step process for it to become feasible as described by Eq. **1** in terms of the free energy change of formation of H_2O ($\Delta G^{H_2O}_{f,T_{oxd}}$) and the entropy of O_2 ($S^{O_2}_{T_{red}}$). Increasing T_{red} increases $S^{O_2}_{T_{red}}$, so the decrease in ΔT window can be permitted at higher T_{red} (7). Conversely, at lower T_{red}, ΔT has to be higher (7):

$$\Delta T = T_{red} - T_{oxd} = -2\Delta G^{H_2O}_{f,T_{oxd}} \Big/ \left(S^{O_2}_{T_{red}}\right). \quad [1]$$

Thermal reduction of the oxide and H_2O splitting have been conducted at the same temperature ($T_{red} = T_{oxd} = T_{iso}$) in which the large pressure swing in the gas composition between reduction and oxidation processes acts as the driving force (15).

Splitting of CO_2 is analogous to that of H_2O and releases a stoichiometric quantity of CO, making this process useful for the

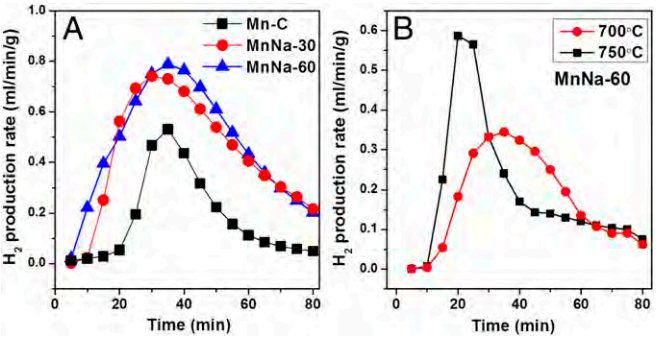

Fig. 2. H_2 evolution plots of reaction of Mn_3O_4 with Na_2CO_3 at (*A*) 850 °C and (*B*) 750 °C and 700 °C. Bulk and ball-milled Mn_3O_4 + Na_2CO_3 are designated as Mn-C and MnNa, respectively. The 30 and 60 represent ball milling times in minutes. Reproduced with permission from ref. 13, copyright 2016, Royal Society of Chemistry.

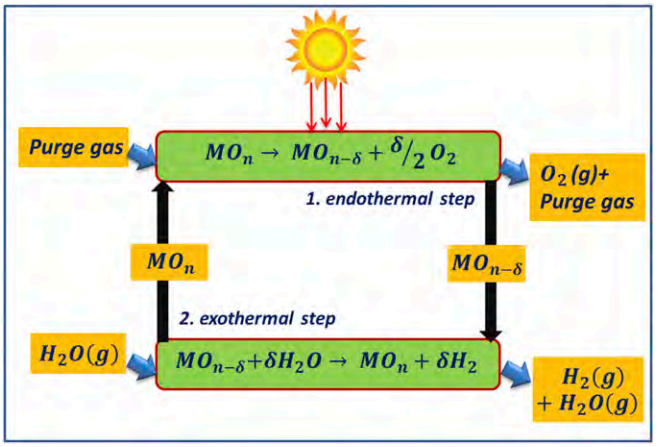

Fig. 3. Schematic representation of the two-step solar thermochemical splitting of H_2O using nonstoichiometric metal oxide redox pairs and concentrated solar energy. During the endothermal reaction, the metal oxide (MO_n) reduces to oxygen-vacant $MO_{n-\delta}$ with the evolution O_2(g) along with inert gas. In the exothermal step, $MO_{n-\delta}$ takes back oxide ions from H_2O and goes back to initial MO_n for cycling with the evolution of H_2(g).

production of syngas (H_2+CO+CO_2) that can be converted into a liquid fuel as the end product. In view of the global climate change due to CO_2 emission, splitting of CO_2 provides an additional means of cutting its concentration. The important distinction between CO_2 and H_2O splitting is as follows. Above 1,100 K, CO_2 splitting is thermodynamically more favored and gets kinetic advantages of reduction. The water–gas shift reaction ($WGS: H_2O + CO \rightarrow CO_2 + H_2$) and the reverse water–gas shift reaction ($RWGS: H_2 + CO_2 \rightarrow CO + H_2O$) appear as alternative approaches to liquid fuel production via syngas production. H_2 production through the low-temperature WGS reaction is thermodynamically favorable due to this cross-over in stability. Maravelias and coworkers (16, 17) assessed the three main thermochemical fuel production systems shown in Fig. S2. In these systems, syngas is produce via (*i*) solar CO_2 splitting followed by the WGS reaction, (*ii*) solar H_2O splitting followed by the RWGS reaction, and (*iii*) splitting of CO_2 and H_2O without the WGS/RWGS reaction. The loss of efficiency of systems *i* and *ii* is due to the energy-intensive CO_2/CO separation and to the unfavorable thermodynamics of the RWGS reaction, respectively. The efficiency of system *iii* is greater than that of the other two because the requirement of CO_2/CO separation is reduced significantly and the H_2:CO ratio is set by the distribution of the solar heating units (16, 17).

Two-step cycles can make use of stoichiometric or nonstoichiometric oxides. Stoichiometric oxides can be volatile and nonvolatile oxides during the redox process. Typical volatile cycles are ZnO/Zn, SnO/SnO_2, In_2O_3/In, and CdO/Cd redox pairs that exhibit reversible solid–gas phase transitions during cycling. Volatile cycles are thermodynamically favorable due to the high entropic gain related to the formation of the gaseous product during the reduction (18). Recombination of product gases is a practical challenge in these cycles and needs to be addressed. In nonvolatile cycles, the redox pairs remain in the condensed state and bypass the problems of product recombination. The Fe_3O_4/FeO cycle, first reported by Nakamura (19), operates at 2,500 K. The melting point of Fe_3O_4 (1,870 K) and FeO (1,650 K) is lower than the reduction temperature of Fe_3O_4, which results in severe coarsening of particles and further deactivates the cycles due to the alternating fusion and solidification of iron oxides (20). To lower the reduction temperature further, divalent metal ions (M = Zn, Ni, Co, Mg, and Mn) were incorporated in the Fe_3O_4 matrix to form mixed ferrites ($M_xFe_{3-x}O_4$) (9, 21). Incorporation of Co and Ni improves the reduction capability of ferrites substantially. Notably, NiO (melting point of 2,271 K) incorporated in the Fe_3O_4 matrix boosts the performance (21, 22). Slow Fe^{2+} diffusion retards the redox activity of ferrites. To overcome this limitation, either nanostructuring of iron oxides or introduction of additional supports (YSZ, ZrO_2, CaSZ, etc.) has been proposed (23). Nanostructuring has been carried out by atomic layer deposited $CoFe_2O_4$ and $NiFe_2O_4$ on high surface area Al_2O_3 to improve the reaction kinetics (24). However, because coarsening of ferrite particles is a matter of concern, nanostructuring is not a practical solution. Addition of supports improves the reaction kinetics and solves the sintering of ferrite particles, although it is also not the ideal solution because of heat loss due to the high mass percentages of supports.

Nonstoichiometric oxide cycles are nonvolatile. In step 1 (Fig. 3), thermal reduction generates nonstoichiometric compositions; in step 2, the oxygen vacancies are eliminated by reaction with H_2O or CO_2. The oxygen exchange capacity is dictated by the nonstoichiometry (δ), which further controls the H_2 production as well as $\eta_{solar\text{-}fuel}$. Knowledge of the partial molar enthalpy $\Delta H_{redox}(\delta)$ and the partial molar entropy $\Delta S_{redox}(\delta)$ of oxygen vacancy formation as a function of δ allows us to deduce oxygen nonstoichiometry under different p_{O_2} and T (Eq. **S9**). The equilibrium H_2 yields (n_{H_2}) and the molar ratio of the oxidant (n_{H_2O}) needed for that purpose are obtained from a knowledge of ΔG_{oxd} of reduced oxides and $\Delta G^{H_2O}_{f,T_{oxd}}$ (Eqs. **S10** and **S11**). The solar-to-fuel conversion efficiency is defined by Eq. **2**, where HHV stands for higher heating value of the fuel produced:

$$\eta_{solar-to-fuel} = \frac{HHV_{H_2} n_{H_2}}{Q_{solar} + E_{penalties}}. \qquad [2]$$

Furthermore, the solar input energy (Q_{solar}), which is mainly for heating water (first term) and the redox material from T_{oxd} to T_{red} (second term) as well as creating oxygen nonstoichiometry (third term), depends on solar energy absorption efficiency of receiver reactor (η_{abs}), as shown in Eq. **S12**. Tamaura et al. (25) used Ni-Mn-ferrite–based nonstoichiometric two-step cycles (1,073–1,373 K), but the quantity of H_2 produced was small.

CeO_2 and Doped CeO_2. Chueh et al. (26) and Furler et al. (27) have investigated the two-step cycle based on the reduction of ceria ($CeO_2 \rightarrow CeO_{2-\delta}$). In such a nonstoichiometric cycle oxygen diffusion is higher than the Fe^{2+} diffusion in ferrite cycles, rendering the use of porous monolithic CeO_2 in state-of-the-art solar cavity receivers (26). The Gibbs free energy of $CeO_{2-\delta} \rightarrow CeO_2$ oxidation with H_2O is negative at all accessible temperatures but the drawback is the poor reducibility of CeO_2. CeO_2 has been modified with several metal ions such as divalent Ca, Sr, and Mg (28), trivalent La, Sc, Gd, Y, Cr, and Sm (29, 30), and tetravalent Zr, Ti, Hf, and Sn ions (29). Substitution with Zr^{4+} is found to increase the reduction capability significantly (29, 31). Fig. 4*A* shows how the partial molar Gibbs free energy of oxygen vacancy formation reduces gradually with increasing Zr content in CeO_2. However, the Gibbs free energy of oxidation of Zr-substituted CeO_2 is more positive than that of pure CeO_2, becoming more positive with increasing Zr content (Fig. 4*B*) (32). The effect becomes more pronounced at high oxidation temperatures. An increase in water

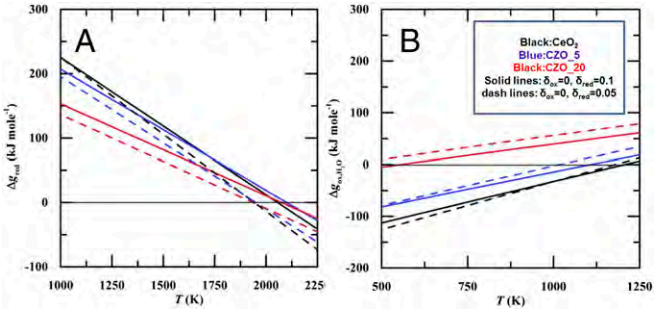

Fig. 4. Gibbs energy change as a function of temperature for the (*A*) reduction and (*B*) oxidation of $Ce_{1-x}Zr_xO_2$ for x = 0 (CeO_2), 0.05 (CZO_5), and 0.2 (CZO_20). Reproduced with permission from ref. 32, copyright 2015, Royal Society of Chemistry.

concentration can promote the complete oxidation of $Zr_xCe_{1-x}O_2$ at all temperatures, but there is an energy penalty (32). A drawback of CeO_2-based oxides is the poor reducibility even at 1,500 °C as well as sublimation of the oxides at high temperatures. Syngas production with CeO_2 by the high temperature two-step cycles has been realized experimentally using the solar cavity receiver setup wherein the variation of the input H_2O:CO_2 molar ratio changes the H_2:CO in the range of 0.25–2.34 (27).

Manganite Perovskites. In perovskite oxides of the type $Ln_{1-x}A_xMnO_3$ ($LnAM_x$), substitution of the trivalent Ln^{3+} by the divalent A^{2+} creates Mn^{3+}/ Mn^{4+} redox active pairs, which assist H_2O splitting in accordance with Eqs. **3** and **4**:

$$Ln_{1-x}A_xMn^{3+}_{1-x}Mn^{4+}_xO_3 \rightarrow Ln_{1-x}A_xMn^{3+}_{1-x+\delta}Mn^{4+}_{x-\delta}O_{3-\delta/2} + \frac{\delta}{4}O_2 \quad [3]$$

$$Ln_{1-x}A_xMn^{3+}_{1-x+\delta}Mn^{4+}_{x-\delta}O_{3-\delta/2} + \frac{\delta}{2}H_2O \rightarrow Ln_{1-x}A_xMn^{3+}_{1-x}Mn^{4+}_xO_3 + \frac{\delta}{2}H_2. \quad [4]$$

High-temperature oxygen nonstoichiometry analysis of $La_{1-x}Sr_xMnO_3$ perovskites by Scheffe et al. (33) obtained by extrapolating the low-temperature experimental nonstoichiometry data estimates the oxygen exchange capacity of $LaSM_x$ perovskites to be higher than that of CeO_2. The use of $La_{1-x}Sr_xMO_3$ (M = Mn, Fe) perovskites for H_2O splitting started with Nalbandian et al. (34), who constructed a membrane reactor consisting of two compartments separated by dense membranes of mixed ionic–electronic perovskites. Rare earth manganite-based H_2O splitting has been investigated thoroughly in recent months.

A-Site Substitution in Manganites. $La_{0.65}Sr_{0.35}MnO_3$ gets reduced to a greater extent than CeO_2 under similar p_{O_2} and temperature, as reported by Scheffe et al. (33). Thermodynamic analysis by Yang et al. (35) predicts superior oxygen exchange capacity of $La_{1-x}Sr_xMnO_3$ (x = 0–0.5) than CeO_2 that further increases with increasing Sr^{2+} substitution, as supported subsequently by thermochemical H_2O splitting resulting in an H_2/O_2 production ratio close to 2. Increasing the Sr^{2+} content decreases the partial molar enthalpy and the entropy of reduction. In other words, the oxidation thermodynamics becomes increasingly unfavorable. In particular, the more positive Gibbs free energy of oxidation of $La_{1-x}Sr_xMnO_{3-\delta}$ relative to $CeO_{2-\delta}$ requires the use of a large excess of H_2O for oxidation (33). Nevertheless, considering the complete heat recovery from H_2O, the $\eta_{solar\text{-}to\text{-}fuel}$ of $LaSM_x$ is predicted to be higher than CeO_2 (33). In this context, it is noteworthy that $La_{1-x}Ca_xMnO_3$ (x = 0.35, 0.5, 0.65) perovskites show an increase in oxygen nonstoichiometry with increasing Ca content, accompanied by a gradual decrease in the reduction temperature (36). A typical thermogravimetric analysis (TGA) plot reveals the oxygen nonstoichiometry generated after reduction (T_{red} = 1,400 °C, 99.9995% Ar) is 2.97, 2.91, and 2.88, respectively, for x of 0.35, 0.5, and 0.65. Although complete reoxidation seems to be difficult with increasing Ca content, $La_{0.5}Ca_{0.5}MnO_3$ (LaCM50) is found to reoxidize stoichiometrically (T_{oxd} = 1,100 °C, p_{CO_2} = 0.4 atm) with almost 1.6 and 5 times higher O_2 and CO production than $La_{0.5}Sr_{0.5}MnO_3$ (LaSM50) and CeO_2, respectively (Fig. 5) (36).

As shown in Fig. 6*A*, in the experiments performed with a laboratory-fabricated furnace, O_2 evolution starts at 1,000 °C with LaCM50 and is complete within 30 min of reaching the plateau near 1,400 °C (99.9995% Ar). O_2 produced by LaCM50 (272 μmol/g) is 1.4 times higher than LaSM50 (193 μmol/g). In particular, LaCM50 produces nearly 42% of O_2 predicted theoretically. The amount of O_2 produced in TGA measurements is slightly higher than that obtained using the laboratory-fabricated furnace due to differences in the reactor dimensions, sample weight, and gas flow rate. Thus, differences in the heat transfer rate and mass diffusion occur, making only a qualitative comparison possible. Interestingly, thermochemical H_2O splitting carried out at 1,000 °C shows the amount of H_2 produced in a span of 100 min by LaCM50 (407 μmol/g) to be greater than that of LaSM50 (308 μmol/g) (Fig. 6*B*). However, H_2 production is not complete even after 100 min and exhibits an extended tail over a long duration (36). The slow kinetics of H_2 evolution can arise due to the decrease in chemical diffusivity, changes in the surface reaction

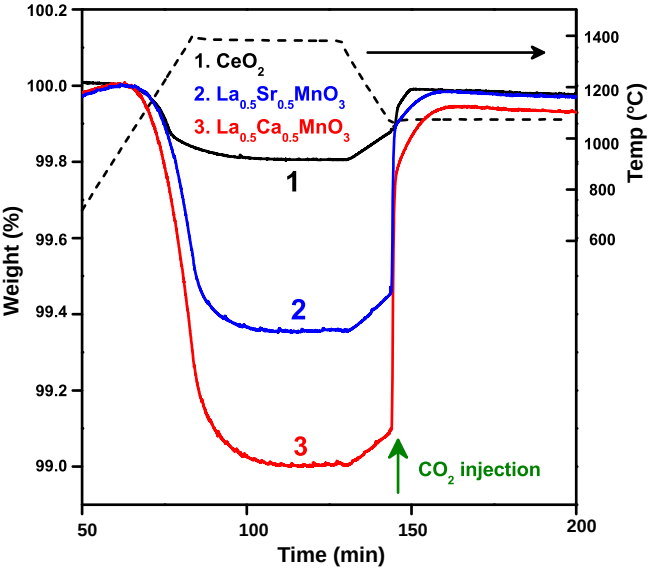

Fig. 5. Representative TGA curves of thermochemical CO_2 splitting of $La_{0.5}Ca_{0.5}MnO_3$ (LaCM 50) in comparison with $La_{0.5}Sr_{0.5}MnO_3$ (LaSM 50) and CeO_2. T_{red} and T_{oxd} are 1,400 °C [99.9995% Ar, flow rate 40 standard cm^3/min (sccm)] and 1,100 °C (pCO_2 = 0.4 atm, flow rate 40 sccm), respectively. Green arrow indicates the point of CO_2 injection. Adapted with permission from ref. 36, copyright 2015, Royal Society of Chemistry. Black arrow indicates change in temperature with time.

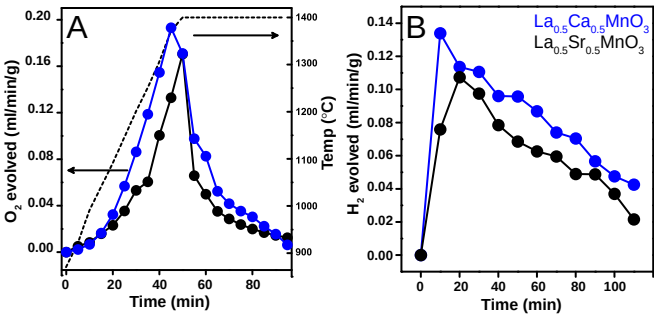

Fig. 6. Rate of (*A*) oxygen (T_{red} = 1400 °C) and (*B*) hydrogen (T_{oxd} = 1,000 °C) production of $La_{0.5}A_{0.5}MnO_3$ (A = Sr, Ca). A laboratory-fabricated furnace was used for this particular measurement. Adapted with permission from ref. 36, copyright 2015, Royal Society of Chemistry. Black arrows indicate change in temperature with time.

constant, and steam concentration as well as the intrinsic thermodynamic driving forces (35). The superior activity of LaCM50 can be related to its crystal structure. Due to the smaller ionic radii of Ca^{2+} in comparison with Sr^{2+}, the tolerance factor (τ) of LaCM50 (τ = 0.978) is lower relative to LaSM50 (τ = 0.996) which emulates higher structural distortion in LaCM50 and helps to produce a greater amount O_2 as well fuel (36). Thermodynamic analysis by Steinfeld and coworkers (37) based on the extraction of partial enthalpy and entropy for oxygen vacancy formation suggests a higher oxygen exchange capacity of $LaCM_x$ than of $LaSM_x$ and identifies LaCM40 as a promising material. Investigations on $La_{1-x}Ba_xMnO_3$ perovskites shows the production of O_2 as well as fuel production to be similar or somewhat less than that of $LaSM_x$ and $LaCM_x$ perovskites (38).

B-Site Substitution in Manganites. Partially substituted $La_{1-x}Sr_xFeO_3$ with transition metals such as Cr, Co, Ni, and Cu has been investigated for syngas production using CH_4 and H_2O as reactants (34, 39). McDaniel et al. (40) first reported production of nine times more H_2 by Al-doped $LaSM_x$ than CeO_2 using two-step H_2O splitting. A recent investigation by Demont and Abanades (38) finds almost no increase in the performance of $LaSM_x$ due to Al doping, whereas a significant increment is reported by Steinfeld and coworkers (37, 41). Systematic doping of Al from 25 to 50% to LaSM50 perovskites causes increasing oxygen nonstoichiometry and subsequent fuel production, although the CO:O_2 ratio decreases from 1.5 to 1.2 (42). The performance of the Al-doped sample is stable during multiple cycling. Ga^{3+}- (up to 35%) and Sc^{3+}- (up to 10%) doped LaSM50 has also been examined for the two-step process, as shown in Fig. S3 (T_{red} = 1,400 °C reached at a heating rate of 20 °C/min, 99.9995% Ar; T_{oxd} = 1,100 °C, p_{CO_2} = 0.4 atm). Increasing the amount of the +3 substituents (Al, Ga, and Sc) increases the oxygen nonstoichiometry and shows better performance than the parent LaSM50. The effect of the trivalent ions varies as Sc > Ga > Al (42). Overdoping decreases the fuel production, although CO production with 25% Ga substitution and 5% Sc substitution is, respectively, 1.5 times and 1.7 times that of the parent LaSM50. The Sc^{3+}-doped perovskite shows the best performance due to the enhanced oxygen mobility related to the bigger size of Sc^{3+} and higher structural distortion is further applied for H_2O splitting (Fig. 7) (42, 43). The CO:O_2 ratio decreases upon substitution of 25% Ga (~1.57) as well as 5% Sc (~1.3) in comparison with the undoped perovskites (~1.62). The unfavorable oxidation thermodynamics and slow oxidation kinetics could cause this discrepancy. Sintering of these oxide materials observed during high temperature cycling could be a reason for the slow oxidation rate. The production of O_2 starts at 900 °C and completes within 40 min after reaching 1,400 °C with the total production of 390 μmol/g (percent reduction = 67%). H_2 is detected immediately after the entrance of the H_2O vapor (T_{oxd} = 1,100 °C), with the amount produced in a span of 100 min being ~250 μmol/g and with an extended tail due to the slow kinetics (Fig. 7*B*) (42).

Deml et al. (44) analyzed the performance of $La_{1-x}Sr_xMn_{1-y}Al_yO_3$ perovskites correlating the oxygen vacancy formation energy using density functional theory calculations. Steinfeld and coworkers have shown that Al doping leads to superior oxygen nonstoichiometry and decreases the partial molar enthalpy of vacancy formation compared with the undoped manganites (37, 41). In particular, production of oxygen by Al-doped $LaSM_x$ and $LaCM_x$ is at least two times higher than that of the undoped manganites at lower oxidation temperature ranges (42). Al^{3+} and Sc^{3+} dopants are resistant to carbonate formation, whereas incorporation of Mg^{2+} shows greater resistance to sintering (38, 42, 45). Few other transition metal- (Fe, Co, and Cr) based perovskites also show good fuel production activity (46, 47).

Changing the Rare Earth in the A-Site. Properties of rare earth manganites depend strongly on the rare earth ion in the A site (48, 49). Two series of perovskites, $Ln_{0.5}Sr_{0.5}MnO_3$ and $Ln_{0.5}Ca_{0.5}MnO_3$ (Ln = La, Nd, Sm, Gd, Dy, and Y), have been used for the two-step thermochemical process recently (50). As shown in Fig. S4, O_2 evolution increases on decreasing the size of rare earth ions from La to Y (T_{red} = 1,400 °C, 99.9995% Ar). Yttrium derivative shows the highest O_2 production, the O_2 released by YCM50 and YSM50 being 573 (74% reduction) and 481 μmol/g (77% reduction), respectively (50). The ability of oxygen vacancy formation is correlated with the tolerance factor (τ) of perovskites in Fig. 8. Decreasing the radius of the rare earth ions reduces τ, which in turn increases the lattice distortion with large tilting of the MnO_6 octahedra. A decrease in τ reduces the Mn–O–Mn bond angle as well as the spatial overlap of Mn e_g and O 2pσ orbitals, favoring oxide ions removal (51). Fig. 8A shows that YSM50, with a τ of 0.965, generates oxygen nonstoichiometry of 2.81, much higher compared with LaSM50 (τ = 0.996). YCM50 (τ = 0.948) exhibits a further improvement in oxygen nonstoichiometry, reaching 2.80 (Fig. 8*B*) (50). The O_2 evolution temperature decreases gradually by reducing the size of rare earth ions from La to Y in case of LnSM50 (Fig. S4*A*, *Inset*). Size mismatch between the Ln and A cations (termed as size variance factor, σ^2) induces local disorder in the perovskite structure (52), which helps in the greater displacement of the oxygens from the mean position and can act as the driving force behind easy removal of oxygens at lower temperature. Notably, σ^2 is higher for LnSM50 derivatives than that of LnCM50 and highest for YSM50.

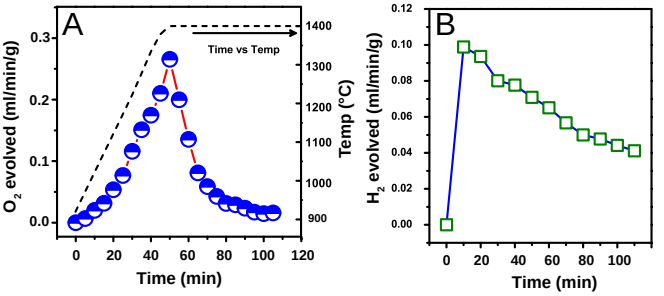

Fig. 7. (*A*) Oxygen (T_{red} = 1400 °C) and (*B*) hydrogen (T_{oxd} = 1,100 °C) evolution profile of $La_{0.5}Sr_{0.5}Sc_{0.05}Mn_{0.95}O_3$. A laboratory-fabricated furnace was used for this particular measurement. Reproduced with permission from ref. 42, copyright 2016, Royal Society of Chemistry.

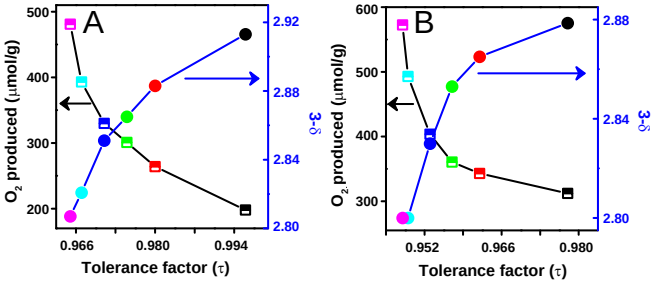

Fig. 8. Variation of O_2 production quantity and oxygen nonstoichiometry generated (3-δ) at 1,400 °C reduction temperature as a function of tolerance factor (τ) of (*A*) $Ln_{0.5}Sr_{0.5}MnO_3$ and (*B*) $Ln_{0.5}Ca_{0.5}MnO_3$ perovskites where Ln = La, Nd, Sm, Gd, Dy, and Y. Adapted with permission from ref. 50, copyright 2015, Wiley-VCH. Black arrows indicate variation of production of O_2 with tolerance factor of perovskites; blue arrows indicate variation of oxygen nonstoichiometry with tolerance factor of perovskites.

Thus, in case of YSM50 ($\sigma^2 = 15.6 \times 10^{-3}$) reduction starts at ~860 °C, whereas YCM50 ($\sigma^2 = 5.6 \times 10^{-3}$) starts to get reduced at ~970 °C (50).

CO produced on splitting CO_2 (T_{oxd} = 1,100 °C, p_{CO_2} = 0.4 atm) is reported to increase with the decrease in the size of the rare earth ion, the highest amount being found with yttrium derivatives. The maximum amount of CO produced by YCM50 (671 μmol/g) at 1,100 °C is even higher than YSM50 (571 μmol/g). Interestingly the oxidation yield of YSM50 increases from 59 to 79% by decreasing the oxidation temperature from 1,100 °C to 900 °C (50). The fuel production activity of YSM50 has been tested during three different reduction/oxidation temperatures (Fig. S5). Production of 624 μmol/g and 418 μmol/g of CO occurred on T_{red}/T_{oxd} of 1,300 °C/900 °C and 1,200 °C/900 °C, respectively, highlighting YSM50 as a potential candidate for energy application (50).

The H_2O splitting activity tested in a tubular furnace also shows that the O_2 evolution of YSM50 begins at a lower temperature than YCM50 (Fig. 9*A*). Satisfactory H_2 production is also obtained with YSM50 and YCM50 with amounts of 320 μmol/g and 310 μmol/g, respectively, in a span of 140 min (Fig. 9*B*). The yield of H_2 during the first 140 min of the reaction arises from the fast kinetic regime, followed by a slower kinetic regime controlled by diffusion (29, 50).

Carbonate Formation. Alkaline earth metals such as Sr and Ca are prone to carbonation during CO_2 exposure. $SrCO_3$ and $CaCO_3$ decompose at ≤940 °C, which indicates that weight gain of nonstoichiometric perovskites on passing CO_2 at lower temperatures (<900 °C) could be partly due to carbonate formation instead of oxidation alone (45). Segregated $SrCO_3$ and $CaCO_3$ on oxide surfaces are found in microscope images (45). In situ X-ray diffraction would monitor the real-time changes of oxides under CO_2 exposure (47). Measuring the produced gases with a gas sensor would be more conclusive. Al^{3+} substitution on $La_{1-x}A_xMnO_3$ (A = Sr, Ca) suppresses the carbonation significantly, as revealed by thermogravimetric analysis (Fig. S6) (45). Sc^{3+} substitution is also effective for this purpose, because it suppresses SrO segregation (42, 53).

Reaction Thermodynamics. From the above discussion it can be surmised that perovskite manganites and Zr-doped CeO_2 exhibit high oxygen yields (n_{O_2}) at low T_{red}. In a practical scenario, $\eta_{solar\text{-}to\text{-}fuel}$ depends extensively on n_{H_2O}/n_{H_2}, reduction enthalpy and entropy of oxide ($\Delta H_{red}, \Delta S_{red}$), $C_{p,redox}$, and ΔT (Eqs. **S9–S12**). Besides $\Delta G^{H_2O}_{f,T_{oxd}}$, these parameters depend on ΔH_{red} and ΔS_{red}, which are inherent properties of the material. We find that (*i*) increasing Zr^{4+} content decreases both the ΔH_{red} and ΔS_{red} of CeO_2. ΔH_{red} linearly decreases as δ reaches nearly 0.075–0.1, but for larger reduction extents it become constant (31, 54) (*ii*) $La_{1-x}Sr_xMnO_3$ perovskites show lower ΔH_{red} than CeO_2 for all compositions. (*iii*) Increasing Sr^{2+} content decreases the ΔH_{red} and ΔS_{red} of $LaMnO_3$ (35). (*iv*) Al^{3+} doping decreases the ΔH_{red} of $La_{1-x}A_xMnO_3$ (A = Sr, Ca), in the higher δ range of 0.075–0.15 (41). On the one hand, decreasing ΔH_{red} favors n_{O_2}, decreases T_{red} (decreases η_{abs}), and favors high $\eta_{solar\text{-}to\text{-}fuel}$. On the other hand, decreasing ΔH_{red} also disfavors ΔG_{oxd} (Eqs. **S9–S12**) and increases the need of n_{H_2O}/n_{H_2} and ΔT (low T_{oxd}), thereby lowering $\eta_{solar\text{-}to\text{-}fuel}$. Manganites favor the reduction thermodynamics whereas CeO_2 favors the oxidation thermodynamics. To design a material that satisfies both the reduction and oxidation thermodynamics seems difficult.

Reaction Kinetics. Generally, the reduction profile is initially rapid followed by a long extended tail, independent of the oxide. This is determined solely by the heat transfer rate rather than by the kinetics of oxygen diffusion or surface reactions (26). In contrast, H_2O splitting kinetics varies with the oxidation thermodynamics (ΔH^0_{oxd}) and the oxide composition. $\eta_{solar\text{-}to\text{-}fuel}$ depends on the upper limit of thermodynamic fuel production, considering infinite amount of gas supply and reaction time, but in practice, however, t_{red} and t_{oxd} need to be optimized (55). (*i*) For CeO_2, $t_{oxd} << t_{red}$ and oxidation completes in 1–2 min whereas the H_2 production time of $La_{1-x}Sr_xMnO_3$ increases monotonically with increasing the Sr content and can take even more than 1 h for x = 0.4, which results in deviation of H_2:O_2 from 2 (35). Near stoichiometric or slight excess n_{H_2O} is enough to reach the target amount of H_2 for CeO_2, although it can be a few orders higher in the case of $La_{1-x}Sr_xMnO_3$ and increases with x (Fig. S7) (35). Thus, CeO_2 has a high theoretical $\eta_{solar\text{-}to\text{-}fuel}$ compared with $La_{1-x}Sr_xMnO_3$ (x > 0.2) at all temperature ranges. Scheffe et al. (33) found that with excess n_{H_2O} input and 100% heat recuperation manganites can surpass the efficiency of CeO_2. (*ii*) The CO production rate is sluggish on increasing Ca content, as in $La_{0.35}Ca_{0.65}MnO_3$ (36). (*iii*) Decreasing the size of the lanthanide retards the oxidation kinetics further. Slow oxidation of $Y_{0.5}Ca_{0.5}MnO_3$ decays the CO:O_2 significantly in comparison with $La_{0.5}Ca_{0.5}MnO_3$ (50). (*iv*) Substitution with +3 ions (Al, Ga, and Sc) slows down the oxidation kinetics, resulting in a CO:O_2 ratio less than 2 (42). It seems difficult to ascertain that slow oxidation is solely due to kinetic or thermodynamic limitations.

Bulk oxygen diffusion and surface reaction are factors that control the reaction kinetics of mixed ionic–electronic conductors. The chemical

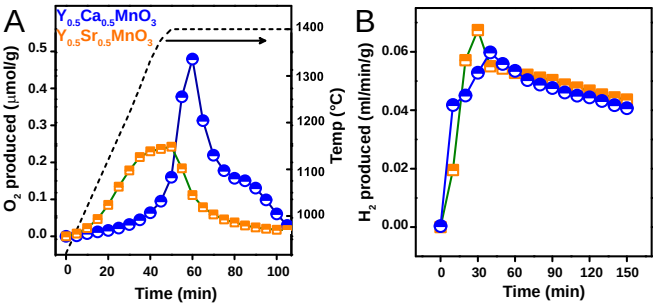

Fig. 9. (*A*) Oxygen (T_{red} = 1,400 °C) and (*B*) hydrogen (T_{oxd} = 1,100 °C) evolution profiles of $Y_{0.5}A_{0.5}MnO_3$ (A = Sr, Ca). A laboratory-fabricated furnace was used for this particular measurement. Adapted with permission from ref. 50, copyright 2015, Wiley-VCH. Black arrow indicates change in temperature with time.

diffusivity (D_{chem}, Eq. **S13**) and chemical surface exchange constant (k_s, Eq. **S14**) are measured by conductivity relaxation or potentiostatic step methods (56, 57). D_{chem} of CeO_2 is nearly 2×10^{-5} cm^2/s (1,073 K). Yasuda and Hishinuma (56) found that D_{chem} of $La_{0.8}Sr_{0.2}MnO_3$ ($\sim 8\times10^{-6}$ cm^2/s at 1,173 K and $\sim 3\times10^{-5}$ cm^2/s at 1,273 K) is lower than CeO_2. Belzner et al. (57) found an order of magnitude decrease in D_{chem} with increasing Sr content from 0.2 to 0.5 due to the oxygen activity variation. D_{chem} of $La_{0.5}Sr_{0.5}MnO_3$ is around 10^{-7} cm^2/s (1,073 K), which renders the characteristic diffusion time of <1 s for the diffusion length (l) of 3–5 μm (diffusion time, $\tau = l^2/4D_{chem}$). The oxidation rate is thus limited by surface reaction rather than bulk oxygen diffusivity. The variation k_s with Sr content remains inconclusive, k_s being sensitive to the gaseous atmosphere. Thus, k_s of $Sm_{0.15}Ce_{0.85}O_{1.925-\delta}$ in a CO–CO_2–Ar mixture is 40 times higher than in an H_2–H_2O–Ar mixture due to kinetic benefits of CO_2 splitting (58). Deposition of Rh on the surface or increasing the surface area enhances the surface reaction rate (59, 60).

Light and Heat Penetration. Microporous structures (felt and monolith) show rapid oxidation due to high surface area. Average and peak $\eta_{solar\text{-}to\text{-}fuel}$ of 0.4% and 0.7% have been obtained by monolith, porous CeO_2 for H_2O splitting (26), whereas CeO_2 felt gives 0.15% and 0.31% for simultaneous splitting of H_2O and CO_2 (27). These structures are opaque to incident radiation, causing a temperature gradient across the thickness of CeO_2 and retards the reduction rate. In contrast, macroporous structures (foam and honeycomb) have pores in the millimeter range through which deeper, volumetric absorption of solar radiation results in homogenous temperature distribution, although their low surface area retards the oxidation rate. Three-dimensional ordered CeO_2 macroporous structures with interconnected pores show a higher CO_2 splitting rate (>1.5 times) than a nonordered entity (61). To accommodate dual-scale porosity (millimeters and micrometers) reticulated porous ceramic (RPC) CeO_2 has been fabricated, resulting in the highest average and peak $\eta_{solar\text{-}to\text{-}fuel}$ of 1.73% and 3.53% for CO_2 splitting (62, 63). The optical thickness of RPC (ε = 280 m^{-1}) is two orders lower than monolith structure (ε = 40,000 m^{-1}) (62). The higher mass loading leads to 17 times more CO production of RPC than the felt in spite of its slow oxidation rate (27, 62). Perovskite oxides of dual-scale porosity have been used in solid oxide fuel cells and have yet to be used for thermochemical splitting of H_2O/CO_2.

Isothermal Cycle

Single-step splitting of H_2O would seem to be the best pathway but the reaction is thermodynamically unfavorable below 4,300 K (1 bar) (9). Thermodynamic considerations demand $T_{red} > T_{oxd}$ for a two-step process (7). Such cyclic rotation between T_{red} and T_{oxd} is accompanied by irreversible heat and time losses and creates thermal stresses on the system. In this context, it is desirable to use isothermal splitting of H_2O (ITWS) which depends on the large pressure swing in the gas composition between reduction and oxidation processes. Fig. S8*A*, based on Eq. **5**, shows that an ideal isothermal cycle must operate either at high T_{red}, low reduction p_{O_2} or at high p_{H_2O}/p_{H_2} (64):

$$T_{iso} = \frac{-\Delta H^0}{R\left(\ln p_{O_2}^{1/2} - \ln \frac{p_{H_2O}}{p_{H_2}}\right) - \Delta S^0}. \quad [5]$$

First, altering any one of these three parameters results in a penalty from others for maintaining $\eta_{solar\text{-}to\text{-}fuel}$, irrespective of the material or the reactor. Second, water thermodynamics dictates that the fuel production per cycle of ITWS is less than two-step splitting of H_2O (TSWS) (Fig. S8*B*). Third, ITWS requires a much higher ratio of fluid input (sweep gas and water vapor) to output products (O_2 and H_2) than TSWS, causing an energy penalty (65). A pumping process has been suggested as an alternative to sweep gas flow but experimental investigations are pending (64, 66). The calculated efficiency of ITWS remains lower than the TSWS (59, 64). ITWS has its own list of advantages. Due to the absence of sweeping between T_{red} and T_{oxd}, the efficiency of ITWS does not depend on solid-state heat recovery (SSHR), which not only makes the reactor concept simple but also releases mechanical and thermal stresses. Thermodynamic analysis of ITWS of CeO_2 suggests a $\eta_{solar\text{-}fuel}$ of 10% (65). Time is the savior in ITWS considering the global reaction rates (55, 59). In this context, the H_2 production rate of CeO_2 at 1,500 °C (9.2 $mL\cdot g^{-1}\cdot h^{-1}$) is not less than the rate predicted for TSWS (59). Finally, high temperature operation of ITWS should minimize the kinetic barrier of oxidation (15). Recent findings of Davenport et al. (67) show that isothermal cycling of CeO_2 at 1,500 °C is limited only by thermodynamic constraints.

Poor reducibility restricts the application of CeO_2 at <1,500 °C. Sublimation of CeO_2 and radiative power loss hinder the application even at high isotherm (>1,500 °C) (55). $La_{1-x}Sr_xMnO_3$ (x = 0–0.5) and YSM50 have been used for isothermal decomposition of CO_2 (ITCS) (Fig. 10) and their performance is superior to CeO_2 even at 1,300 °C (reduction under $p_{O_2} = 10^{-5}$ atm; $p_{CO_2} = 1.0$ atm) (68). The first cycle establishes the equilibrium nonstoichiometry under CO_2 and from the second cycle onward the CO:O_2 ratio is nearly 2 (Fig. 10*A*). The low-temperature performance of manganites requires higher p_{H_2O}/p_{H_2} and a greater need of fluid state heat recovery (FSHR) than CeO_2 (Eq. **5**). Manganites are going to get more benefit from high temperature ITWS due to the more sluggish oxidation kinetics than CeO_2. Above 1,100 K, ITCS yields more fuel than ITWS (Ellingham diagram). Simultaneous variation of both p_{O_2} and temperature is recommended independent of the materials. Neither TSWS nor ITWS near isothermal is estimated to score the highest $\eta_{solar\text{-}fuel}$ (64).

Solar Reactor Technologies

Use of the solar thermal route for H_2O/CO_2 splitting crucially depends on the availability of suitable solar reactors. Construction

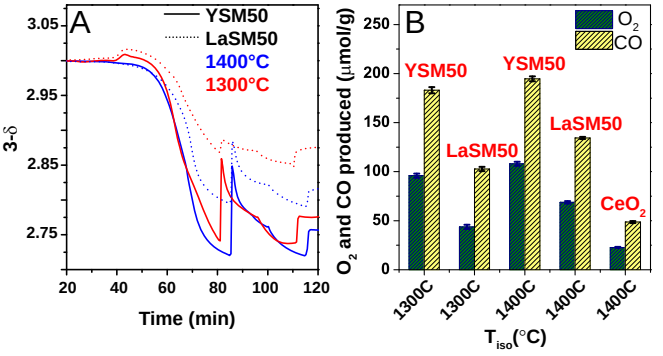

Fig. 10. (*A*) Isothermal CO_2 splitting profile of $Ln_{0.5}Sr_{0.5}MnO_3$ where Ln are Y (solid line) and La (dotted line) for isotherms of 1,400 °C (blue) and 1,300 °C (red). Reduction and oxidation are performed under $pO_2 = 10^{-5}$ atm and $pCO_2 = 0.4$ atm, respectively. (*B*) Histogram quantifies the production of gases by $Ln_{0.5}Sr_{0.5}MnO_3$ in comparison with CeO_2 standard (1,400 °C). Adapted with permission from ref. 68, copyright 2016, American Chemical Society.

of solar reactor to satisfy the operational need of different kind of cycles, materials, and temperature regimes has been discussed elaborately in a few reviews (9, 69, 70). In the case of solar reactors implemented for nonstoichiometric oxide-driven, nonvolatile, two-step cycles, the solar configuration must consist of three basic parts: concentrators, receiver, and reactor. The use of an indirect and direct receiver reactor is discussed in detail in *Supporting Information*. The oxides can be placed either as regular monoliths (structured reactors) or assembled in a packed/fluidized bed (nonstructured reactors) to promote uniform heat and mass transfer as discussed in *Supporting Information* (2, 66, 71, 72). Most of the reactor concepts are devoid of SSHR facilities. Ferrites have been investigated extensively using solar irradiation and there are a few attempts to use CeO_2 in solar reactors. Perovskite oxides have not been executed so far in solar reactors for two-step H_2O/CO_2 splitting purposes.

Future Outlook and Conclusions

The preceding discussion of the solar thermochemical route of generating hydrogen by splitting water should suffice to convince one that it is indeed a viable method for this important process. There are many challenges and opportunities in this area. Thus, it would be necessary to carry out a large-scale experiment on generating hydrogen by the low-temperature, multistep thermochemical cycle based on Mn(III)/Mn (II) oxides. Investigation of an energy-saving pathway for $NaMnO_2$ conversion to Mn_3O_4 is desirable. This is because of the attractive temperature at which H_2 is obtained.

It would be desirable to set up a pilot plant for generating CO and H_2 from CO_2 and H_2O, respectively. Syngas so produced can be useful for generating organics. The applicability of the two-step or the isothermal cycle depends on SSHR and FSHR, respectively. A reactor that minimizes heat loss through radiation or conduction and avoids a quartz window is desirable. Rare earth manganites would be ideal for the low-temperature reduction process. However, the oxidation thermodynamics of ceria is much superior. It may be useful to explore other oxide materials for the two-step process for a tradeoff between the reduction and oxidation reactions. Thermodynamic analysis of various oxides should be carried out for preliminary materials screening. In practice, efficiency should be calculated taking the reaction kinetics into account. The use of reactant gases should be minimized or their separation from product gases should have to be energy-efficient. Successful integration of vacuum pumping of the reactor should be undertaken. Clever design of solar reactors and use of porous materials can overcome heat transfer-limited reduction. Rapid oxidation kinetics and longevity of materials need to be demonstrated for a large number of cycles. Near isothermal performance with the optimization of temperature difference and of the partial pressures of gases should be carried out, especially with manganite-based perovskites.

Acknowledgments

S.D. thanks the Council of Scientific Industrial Research for a fellowship and Sheik Saqr Laboratory for a student fellowship.

1 Herron JA, Kim J, Upadhye AA, Huber GW, Maravelias CT (2015) A general framework for the assessment of solar fuel technologies. *Energy Environ Sci* 8:126–157.
2 Smestad GP, Steinfeld A (2012) Review: Photochemical and thermochemical production of solar fuels from H_2O and CO_2 using metal oxide catalysts. *Ind Eng Chem Res* 51:11828–11840.
3 Rao CNR, Lingampalli SR, Dey S, Roy A (2016) Solar photochemical and thermochemical splitting of water. *Philos Trans A Math Phys Eng Sci* 374:20150088.
4 Rao CNR, Dey S (2016) Generation of H_2 and CO by solar thermochemical splitting of H_2O and CO_2 by employing metal oxides. *J Solid State Chem* 242:107–115.
5 Beghi GE (1986) A decade of research on thermochemical hydrogen at the Joint Research Centre, Ispra. *Int J Hydrogen Energy* 11:761–771.
6 Yalccin S (1989) A review of nuclear hydrogen production. *Int J Hydrogen Energy* 14:551–561.
7 Meredig B, Wolverton C (2009) First-principles thermodynamic framework for the evaluation of thermochemical H_2O - or CO_2-splitting materials. *Phys Rev B* 80:245119.
8 Xu B, Bhawe Y, Davis ME (2012) Low-temperature, manganese oxide-based, thermochemical water splitting cycle. *Proc Natl Acad Sci USA* 109:9260–9264.
9 Kodama T, Gokon N (2007) Thermochemical cycles for high-temperature solar hydrogen production. *Chem Rev* 107:4048–4077.
10 Sturzenegger M, Nuesch P (1999) Efficiency analysis for a manganese-oxide-based thermochemical cycle. *Energy* 24:959–970.
11 Tamaura Y, et al. (1998) Thermodynamic evaluation of water splitting by a cation-excessive (Ni, Mn) ferrite. *Int J Hydrogen Energy* 23:1185–1191.
12 Kaneko H, et al. (2001) Enhancement of O_2-releasing step with Fe_2O_3 in the water splitting by $MnFe_2O_4$-Na_2CO_3 system. *J Phys Chem Solids* 62:1341–1347.
13 Dey S, Rajesh S, Rao CNR (2016) Significant reduction in the operating temperature of the Mn (II)/Mn (III) oxide-based thermochemical water splitting cycle brought about by the use of nanoparticles. *J Mater Chem A Mater Energy Sustain* 4:16830–16833.
14 Xu B, Bhawe Y, Davis ME (2013) Spinel metal oxide-alkali carbonate-based, low-temperature thermochemical cycles for water splitting and CO_2 reduction. *Chem Mater* 25:1564–1571.
15 Muhich CL, et al. (2013) Efficient generation of H_2 by splitting water with an isothermal redox cycle. *Science* 341:540–542.
16 Kim J, et al. (2011) Methanol production from CO2 using solar-thermal energy: Process development and techno-economic analysis. *Energy Environ Sci* 4:3122–3132.
17 Kim J, Johnson TA, Miller JE, Stechel EB, Maravelias CT (2012) Fuel production from CO2 using solar-thermal energy: system level analysis. *Energy Environ Sci* 5:8417–8429.
18 Scheffe JR, Steinfeld A (2014) Oxygen exchange materials for solar thermochemical splitting of H_2O and CO_2: A review. *Mater Today* 17:341–348.
19 Nakamura T (1977) Hydrogen production from water utilizing solar heat at high temperatures. *Sol Energy* 19:467–475.
20 Steinfeld A, Sanders S, Palumbo R (1999) Design aspects of solar thermochemical engineering-a case study: Two-step water-splitting cycle using the Fe_3O_4/FeO redox system. *Sol Energy* 65:43–53.
21 Gokon N, Murayama H, Nagasaki A, Kodama T (2009) Thermochemical two-step water splitting cycles by monoclinic ZrO_2-supported $NiFe_2O_4$ and Fe_3O_4 powders and ceramic foam devices. *Sol Energy* 83:527–537.
22 Allendorf MD, Diver RB, Siegel NP, Miller JE (2008) Two-step water splitting using mixed-metal ferrites: Thermodynamic analysis and characterization of synthesized materials. *Energy Fuels* 22:4115–4124.
23 Gokon N, Murayama H, Umeda J, Hatamachi T, Kodama T (2009) Monoclinic zirconia-supported Fe_3O_4 for the two-step water-splitting thermochemical cycle at high thermal reduction temperatures of 1400-1600 C. *Int J Hydrogen Energy* 34:1208–1217.
24 Arifin D, Aston VJ, Liang X, McDaniel AH, Weimer AW (2012) $CoFe_2O_4$ on a porous Al_2O_3 nanostructure for solar thermochemical CO_2 splitting. *Energy Environ Sci* 5:9438–9443.
25 Tamaura Y, Steinfeld A, Kuhn P, Ehrensberger K (1995) Production of solar hydrogen by a novel, 2-step, water-splitting thermochemical cycle. *Energy* 20:325–330.
26 Chueh WC, et al. (2010) High-flux solar-driven thermochemical dissociation of CO_2 and H_2O using nonstoichiometric ceria. *Science* 330:1797–1801.
27 Furler P, Scheffe JR, Steinfeld A (2012) Syngas production by simultaneous splitting of H_2O and CO_2 via ceria redox reactions in a high-temperature solar reactor. *Energy Environ Sci* 5:6098–6103.
28 Kang M, et al. (2014) Enhanced thermochemical CO_2 splitting over Mg- and Ca-doped ceria/zirconia solid solutions. *RSC Advances* 4:5583–5590.
29 Scheffe JR, Jacot R, Patzke GR, Steinfeld A (2013) Synthesis, characterization, and thermochemical redox performance of Hf^{4+}, Zr^{4+}, and Sc^{3+} doped ceria for splitting CO_2. *J Phys Chem C* 117:24104–24114.

30 Le Gal A, Abanades S (2012) Dopant incorporation in ceria for enhanced water-splitting activity during solar thermochemical hydrogen generation. *J Phys Chem C* 116:13516–13523.
31 Hao Y, Yang C-K, Haile SM (2014) Ceria-zirconia solid solutions ($Ce_{1-x}Zr_xO_{2-\delta}$, $x \leq 0.2$) for solar thermochemical water splitting: A thermodynamic study. *Chem Mater* 26:6073–6082.
32 Takacs M, Scheffe JR, Steinfeld A (2015) Oxygen nonstoichiometry and thermodynamic characterization of Zr doped ceria in the 1573-1773 K temperature range. *Phys Chem Chem Phys* 17:7813–7822.
33 Scheffe JR, Weibel D, Steinfeld A (2013) Lanthanum-strontium-manganese perovskites as redox materials for solar thermochemical splitting of H_2O and CO_2. *Energy Fuels* 27:4250–4257.
34 Nalbandian L, Evdou A, Zaspalis V (2009) $La_{1-x}Sr_xMO_3$ (M = Mn, Fe) perovskites as materials for thermochemical hydrogen production in conventional and membrane reactors. *Int J Hydrogen Energy* 34:7162–7172.
35 Yang CK, Yamazaki Y, Aydin A, Haile SM (2014) Thermodynamic and kinetic assessments of strontium-doped lanthanum manganite perovskites for two-step thermochemical water splitting. *J Mater Chem A Mater Energy Sustain* 2:13612–13623.
36 Dey S, Naidu BS, Govindaraj A, Rao CNR (2015) Noteworthy performance of $La_{(1-x)}Ca_{(x)}MnO_3$ perovskites in generating H_2 and CO by the thermochemical splitting of H_2O and CO_2. *Phys Chem Chem Phys* 17:122–125.
37 Cooper T, et al. (2015) Lanthanum manganite perovskites with Ca/Sr A-site and Al B-site doping as effective oxygen exchange materials for solar thermochemical fuel production. *Energy Technology* 3:1130–1142.
38 Demont A, Abanades S (2015) Solar thermochemical conversion of CO_2 into fuel via two-step redox cycling of non-stoichiometric Mn-containing perovskite oxides. *J Mater Chem A Mater Energy Sustain* 3:3536–3546.
39 Nalbandian L, Evdou A, Zaspalis V (2011) $La_{1-x}Sr_xM_yFe_{1-y}O_{3-\delta}$ perovskites as oxygen-carrier materials for chemical-looping reforming. *Int J Hydrogen Energy* 36:6657–6670.
40 McDaniel AH, et al. (2013) Sr- and Mn-doped $LaAlO_{3-\delta}$ for solar thermochemical H_2 and CO production. *Energy Environ Sci* 6:2424–2428.
41 Takacs M, et al. (2016) Oxygen nonstoichiometry, defect equilibria, and thermodynamic characterization of $LaMnO_3$ perovskites with Ca/Sr A-site and Al B-site doping. *Acta Mater* 103:700–710.
42 Dey S, Naidu BS, Rao CNR (2016) Beneficial effects of substituting trivalent ions in the B-site of $La_{0.5}Sr_{0.5}Mn_{1-x}A_xO_3$ (A = Al, Ga, Sc) on the thermochemical generation of CO and H_2 from CO_2 and H_2O. *Dalton Trans* 45:2430–2435.
43 Yue X, et al. (2008) Investigation on scandium-doped manganate $La_{0.8}Sr_{0.2}Mn_{1-x}Sc_xO_{3-\delta}$ cathode for intermediate temperaturesolid oxide fuel cells. *J Power Sources* 185:691–697.
44 Deml AM, et al. (2014) Tunable oxygen vacancy formation energetics in the complex perovskite oxide $Sr_xLa_{1-x}Mn_yAl_{1-y}O_3$. *Chem Mater* 26:6595–6602.
45 Gálvez ME, et al. (2015) Physico-chemical changes in Ca, Sr and Al-doped La-Mn-O perovskites upon thermochemical splitting of CO_2 via redox cycling. *Phys Chem Chem Phys* 17:6629–6634.
46 Demont A, Abanades S, Beche E (2014) Investigation of perovskite structures as oxygen-exchange redox materials for hydrogen production from thermochemical two-step water-splitting cycles. *J Phys Chem C* 118:12682–12692.
47 Bork AH, Kubicek M, Struzik M, Rupp JLM (2015) Perovskite $La_{0.6}Sr_{0.4}Cr_{1-x}Co_xO_{3-\delta}$ solid solutions for solar-thermochemical fuel production: Strategies to lower the operation temperature. *J Mater Chem A Mater Energy Sustain* 3:15546–15557.
48 Rao CNR (2000) Charge, spin, and orbital ordering in the perovskite manganates, $Ln_{1-x}A_xMnO_3$ (Ln= rare earth, A= Ca or Sr). *J Phys Chem B* 104:5877–5889.
49 Kharton VV, et al. (2008) Oxygen nonstoichiometry, mixed conductivity, and Mossbauer spectra of $Ln_{0.5}A_{0.5}FeO_{3-d}$ (Ln= La-Sm, A= Sr, Ba): Effects of cation size. *Chem Mater* 20:6457–6467.
50 Dey S, Naidu BS, Rao CNR (2015) $Ln_{0.5}A_{0.5}MnO_3$ (Ln=Lanthanide, A= Ca, Sr) perovskites exhibiting remarkable performance in the thermochemical generation of CO and H_2 from CO_2 and H_2O. *Chemistry* 21:7077–7081.
51 Woodward PM, et al. (1998) Influence of cation size on the structural features of $Ln_{1/2}A_{1/2}MnO_3$ perovskites at room temperature. *Chem Mater* 10:3652–3665.
52 Attfield JP (1998) A simple approach to lattice effects in conducting perovskite-type oxides. *Chem Mater* 10:3239–3248.
53 Zhang C, et al. (2009) A comparative study of La0.8Sr0.2MnO3 and La0.8Sr0.2Sc0.1Mn0.9O3 as cathode materials of single-chamber SOFCs operating on a methane-air mixture. *J Power Sources* 191:225–232.
54 Kuhn M, Bishop SR, Rupp JLM, Tuller HL (2013) Structural characterization and oxygen nonstoichiometry of ceria-zirconia (Ce1-xZrxO2-d) solid solutions. *Acta Mater* 61:4277–4288.
55 Venstrom LJ, De Smith RM, Hao Y, Haile SM, Davidson JH (2014) Efficient splitting of CO_2 in an isothermal redox cycle based on ceria. *Energy Fuels* 28:2732–2742.
56 Yasuda I, Hishinuma M (1996) Electrical conductivity and chemical diffusion coefficient of strontium-doped lanthanum manganites. *J Solid State Chem* 123:382–390.
57 Belzner A, Gur TM, Huggins RA (1992) Oxygen chemical diffusion in strontium doped lanthanum manganites. *Solid State Ion* 57:327–337.
58 Gopal CB, Haile SM (2014) An electrical conductivity relaxation study of oxygen transport in samarium doped ceria. *J Mater Chem A Mater Energy Sustain* 2:2405–2417.
59 Hao Y, Yang CK, Haile SM (2013) High-temperature isothermal chemical cycling for solar-driven fuel production. *Phys Chem Chem Phys* 15:17084–17092.
60 Chueh WC, Haile SM (2010) A thermochemical study of ceria: Exploiting an old material for new modes of energy conversion and CO_2 mitigation. *Philos Trans R Soc A* 368:3269–3294.
61 Rudisill SG, et al. (2013) Enhanced oxidation kinetics in thermochemical cycling of CeO2 through templated porosity. *J Phys Chem C* 117:1692–1700.
62 Furler P, et al. (2012) Solar thermochemical CO2 splitting utilizing a reticulated porous ceria redox system. *Energy Fuels* 26:7051–7059.
63 Furler P, et al. (2014) Thermochemical CO_2 splitting via redox cycling of ceria reticulated foam structures with dual-scale porosities. *Phys Chem Chem Phys* 16:10503–10511.
64 Ermanoski I, Miller JE, Allendorf MD (2014) Efficiency maximization in solar-thermochemical fuel production: Challenging the concept of isothermal water splitting. *Phys Chem Chem Phys* 16:8418–8427.
65 Bader R, Venstrom LJ, Davidson JH, Lipinski W (2013) Thermodynamic analysis of isothermal redox cycling of ceria for solar fuel production. *Energy Fuels* 27:5533–5544.
66 Ermanoski I, Siegel NP, Stechel EB (2013) A new reactor concept for efficient solar-thermochemical fuel production. *J Sol Energy Eng* 135:031002.
67 Davenport TC, Yang C-K, Kucharczyk CJ, Ignatowich MJ, Haile SM (2016) Implications of exceptional material kinetics on thermochemical fuel production rates. *Energy Technol* 4:764–770.
68 Dey S, Rao CNR (2016) Splitting of CO_2 by manganite perovskites to generate CO by solar isothermal redox cycling. *ACS Energy Lett* 1:237–243.
69 Muhich CL, et al. (2015) A review and perspective of efficient hydrogen generation via solar thermal water splitting. *Energy Environ* 5:261–287.
70 Agrafiotis C, Roeb M, Sattler C (2015) A review on solar thermal syngas production via redox pair-based water/carbon dioxide splitting thermochemical cycles. *Renew Sustain Energy Rev* 42:254–285.
71 Miller JE, et al. (2012) Development and assessment of solar-thermal-activated fuel production: Phase 1 summary. Report No. SAND2012-5658 (Sandia National Laboratories, Albuquerque, NM).
72 Gokon N, Mataga T, Kondo N, Kodama T (2011) Thermochemical two-step water splitting by internally circulating fluidized bed of NiFe2O4 particles: Successive reaction of thermal-reduction and water-decomposition steps. *Int J Hydrogen Energy* 36:4757–4767.